

Supplementary Information for

***In situ* X-ray diffraction of silicate liquids and glasses under dynamic and static compression over megabar pressure**

Guillaume Morard^{a,b}, Jean-Alexis Hernandez^{c,d}, Marco Guarguaglini^c, Riccardo Bolis^c, Alessandra Benuzzi-Mounaix^c, Tommaso Vinci^c, Guillaume Fiquet^a, Marzena. A. Baron^a, Sang Heon Shim^e, Byeongkwan Ko^e, Arianna E. Gleason^{f,g}, Wendy L. Mao^f, Roberto Alonso-Mori^g, Hae Ja Lee^g, Bob Nagler^g, Eric Galtier^g, Dimosthenis Sokaras^g, Siegfried H. Glenzer^g, Denis Andrault^h, Gaston Garbarinoⁱ, Mohamed Mezouarⁱ, ~~Anja Schuster~~^j, Alessandra Ravasio^c

Paste manuscript title here

Paste the full author list here

Corresponding author : Guillaume Morard
Email : guillaume.morard@univ-grenoble-alpes.fr

This PDF file includes:

Supplementary text
Figures S1 to S13
Tables S1 to S6
SI References

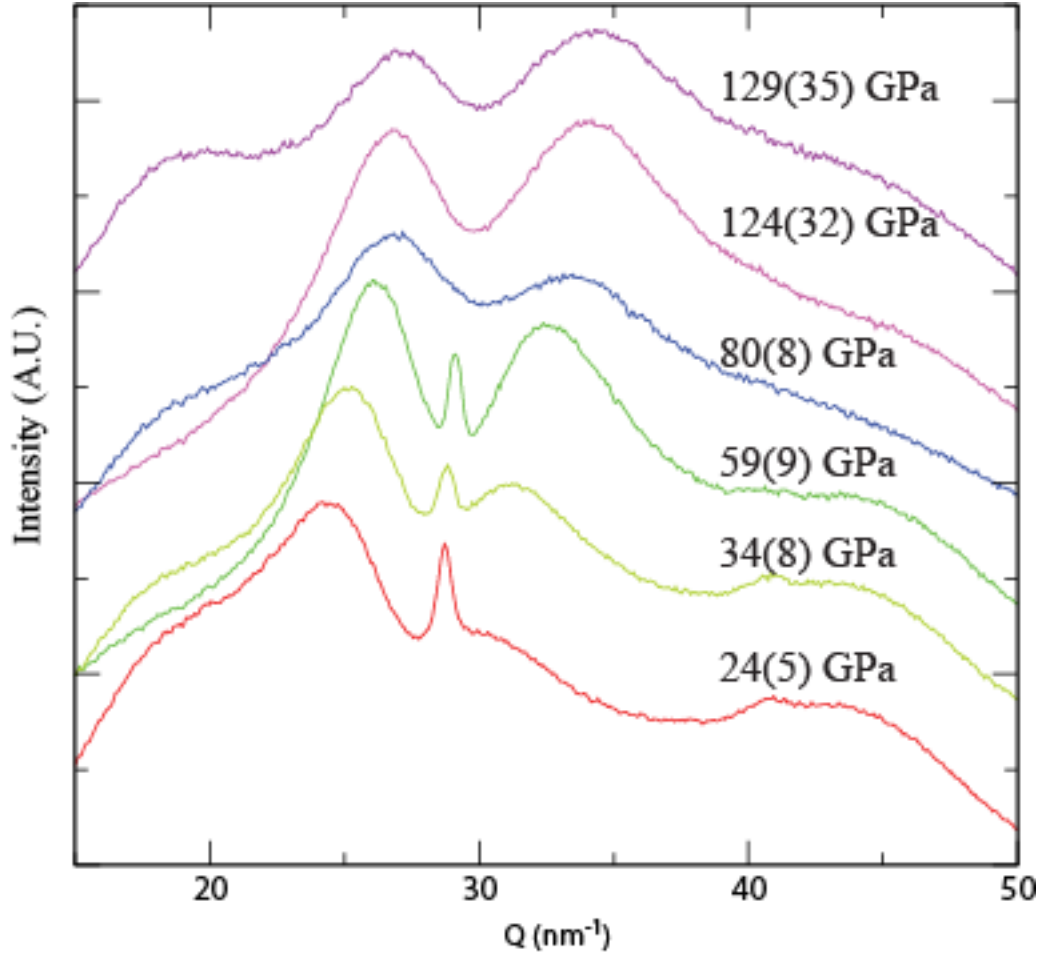


Figure S1: Diffraction spectra of shock compressed MgSiO_3 glasses, before subtraction of cold background. Stars symbols indicate peaks from the Ti coating. On the drive side it prevents the laser to shine through the target and serves as reflecting interface on the VISAR side (**Figure S10**). Signal from the unshocked diffraction pattern has been removed in different proportions to the compressed signal in order to obtain the patterns shown in **Figure 1**.

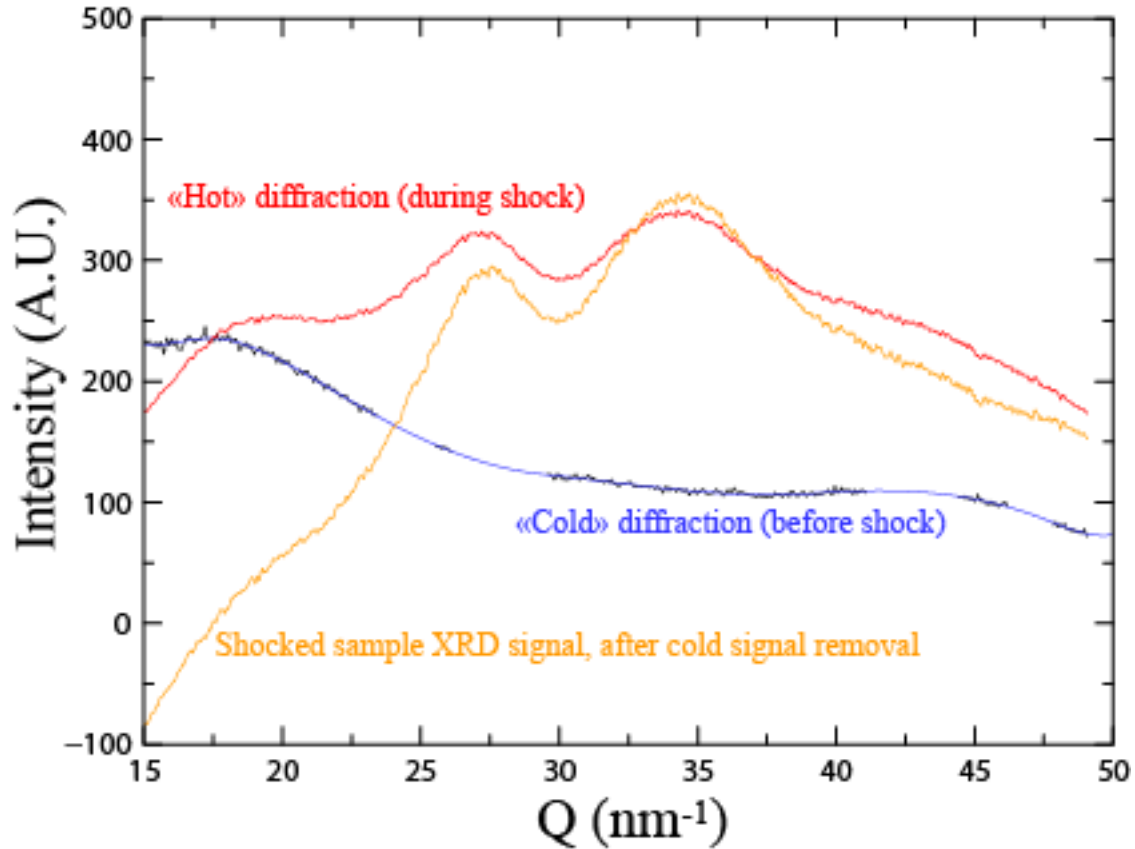


Figure S2: Illustration of background removal procedure for disordered shocked patterns. First, the cold diffraction pattern is recorded before the launch of the laser shock wave. Ti diffraction peaks removed and the signal below these peaks interpolated (blue line). Then, this signal is rescaled following the timing of the XFEL with respect to the shock breakout, which give the proportion of shocked and unshocked material in the X-ray spot. This rescaled pattern is then removed to the “hot” pattern, taken during shock (in red), to obtain the diffraction pattern of the shocked sample only (in orange). A small hump is visible around 20 nm^{-1} related to the polystyrene diffraction placed in front as ablator.

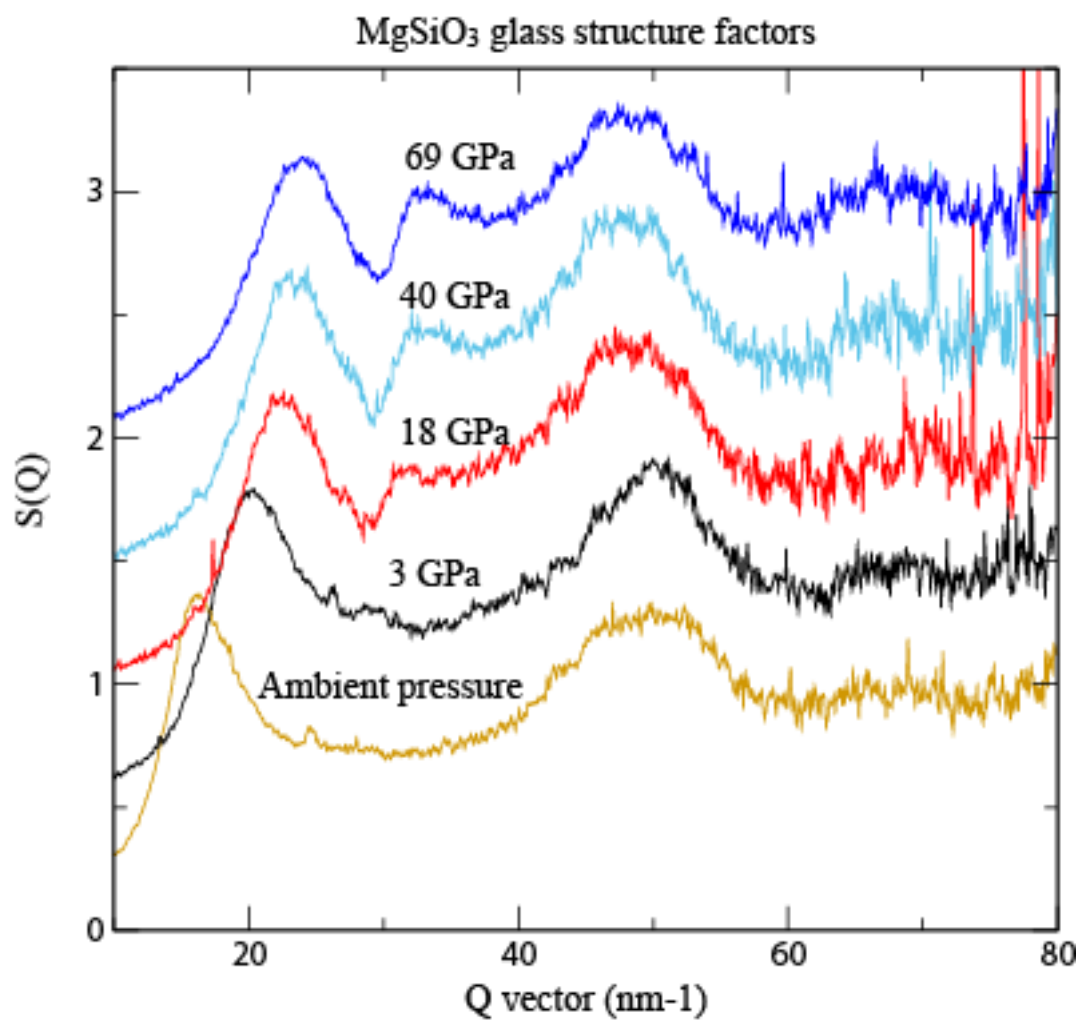


Figure S3: Structure factors $S(Q)$ for MgSiO₃ glasses measured during static compression experiments.

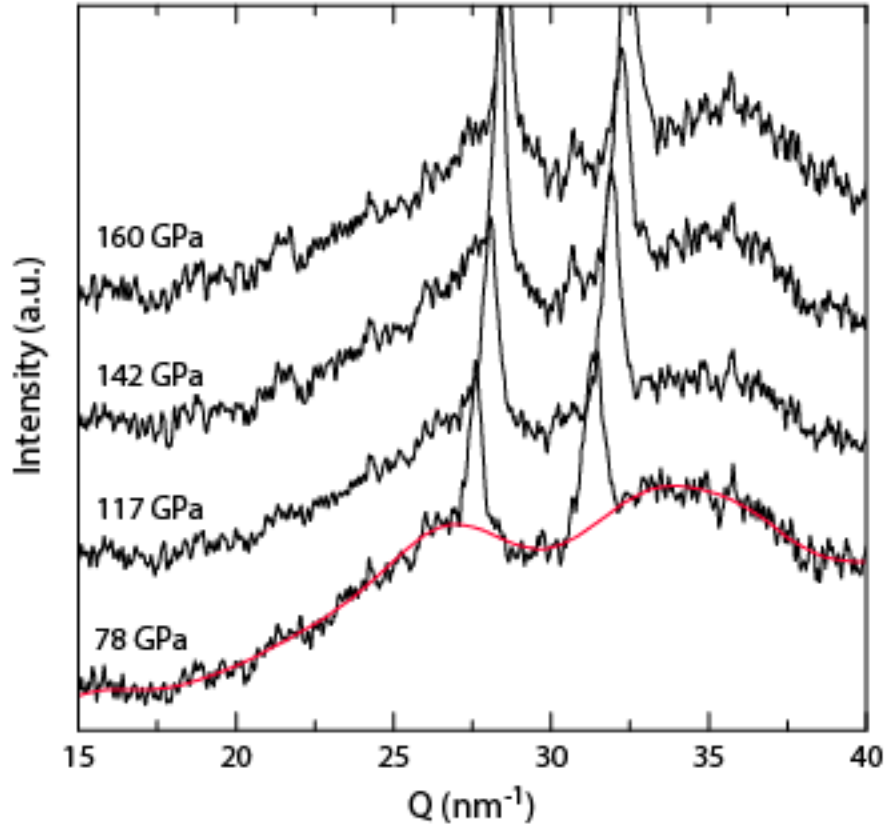


Figure S4 : High pressure XRD patterns of MgSiO_3 glass cold compressed in DAC.

These dataset has been recorded without Sollers slits set-up, contrary to the dataset presented in [Figure 1](#). Diffraction peaks visible here are coming from the surrounding Re gasket and are used to calibrate the pressure, following the EoS of (1). Example of the interpolation used to measure the peak positions $Q1$ and $Q2$ is presented on the first pattern.

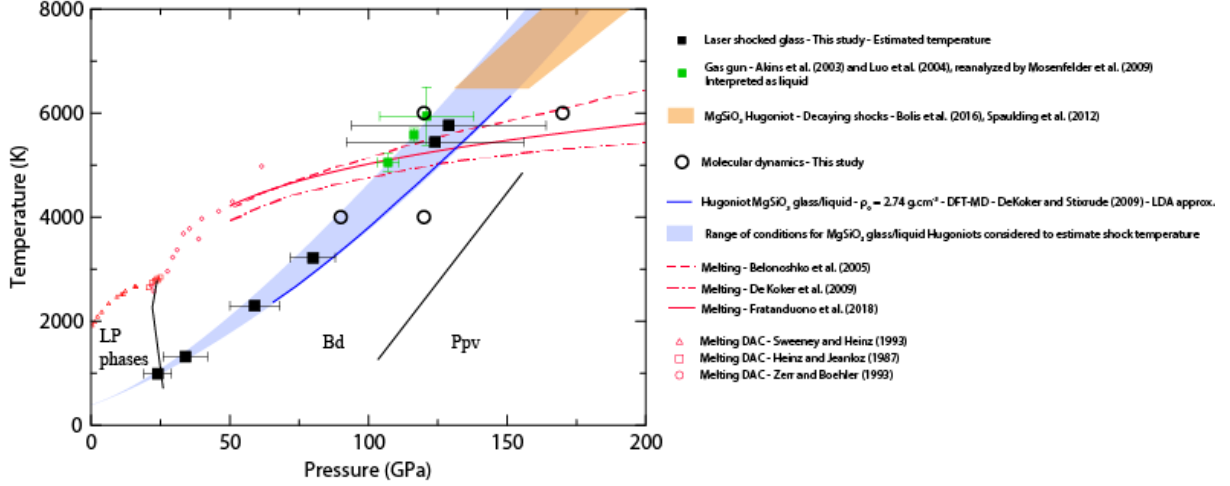


Figure S5: P-T conditions probed for glassy and liquid MgSiO_3 . We estimated the P-T conditions of the glass and liquid formed in our laser-shock experiment (blue area) based on existing Hugoniot measurements performed in the liquid state (2–6) and based on the theoretical Hugoniot of MgSiO_3 glass with shocked states presenting a dense amorphous structure (as measured as ns-scale by XRD our experiment) (7). The different melting curve are based on experimental (8–11) and theoretical works (7, 12). Square symbols indicates the shots performed on MgSiO_3 in this experiment. The two shots at highest pressure are presumed to be in the liquid state. The perovskite post-perovskite phase boundary has been measured in (13).

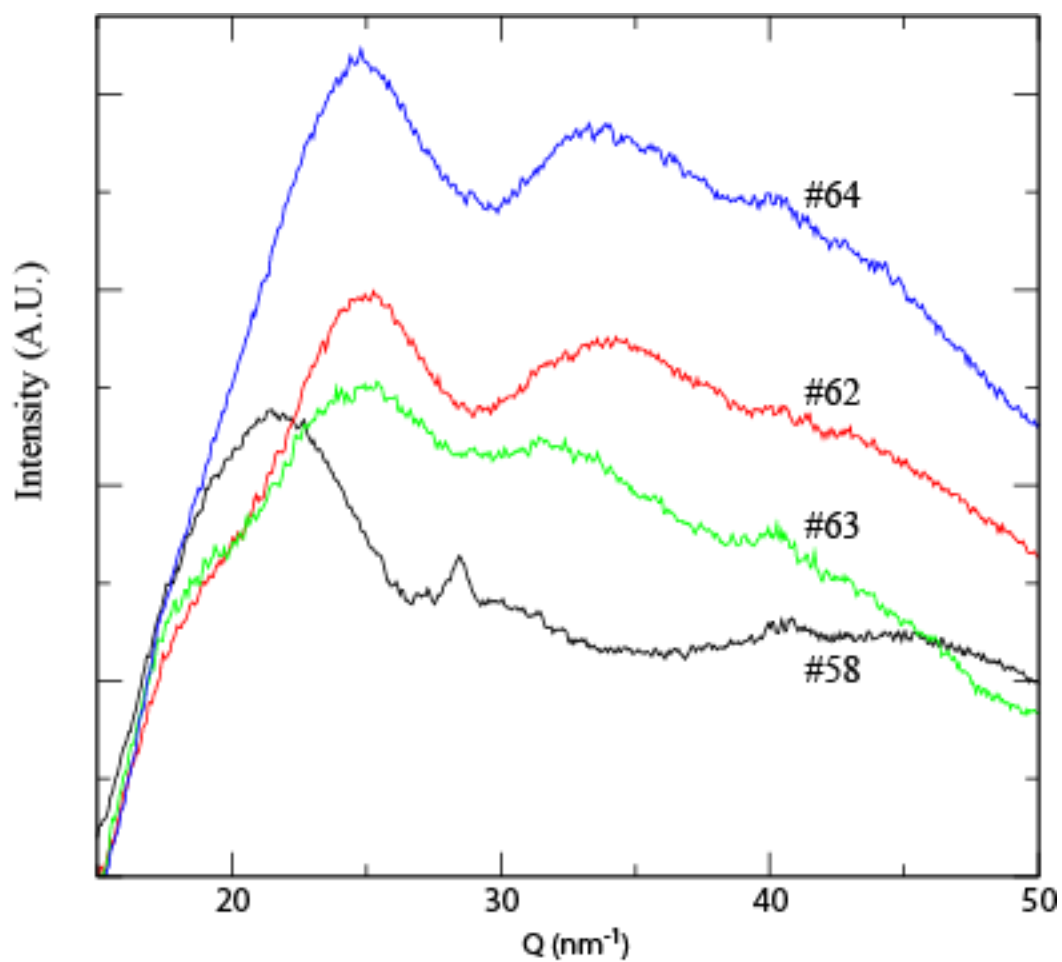


Figure S6: Diffraction patterns of shock compressed liquid SiO₂, obtained using fused silica as starting materials. The pressure, calculated from VISAR measurements, is indicated, as well as a XRD pattern of a target before shock.

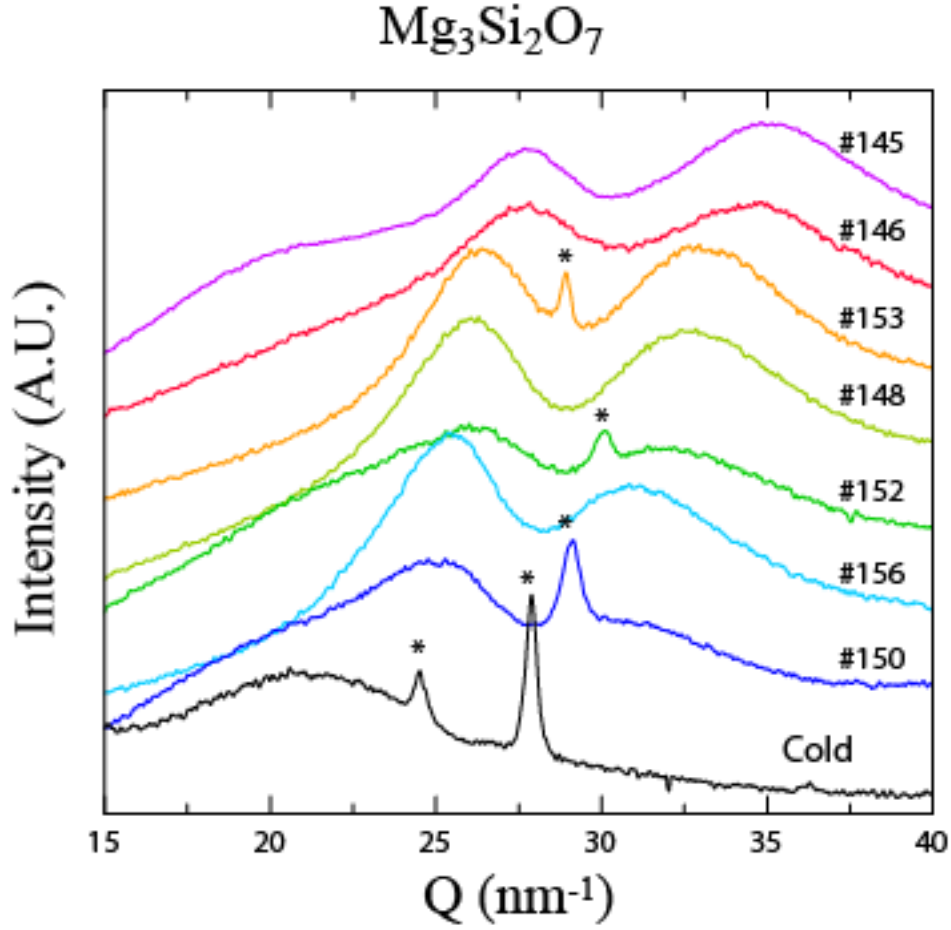


Figure S7: Diffraction patterns for shocked $\text{Mg}_3\text{Si}_2\text{O}_7$ glass samples. The diffraction patterns are arranged as a function of the Q_1 and Q_2 positions. This other glass corresponds to an intermediate composition (40% SiO_2) between MgSiO_3 (50% SiO_2) and Mg_2SiO_4 (33% SiO_2). As no Hugoniot data on this $\text{Mg}_3\text{Si}_2\text{O}_7$ glass is available, relation between Q_1 and Q_2 peak positions and pressure cannot be established. However, the present dataset highlights a similar behavior for Q_1 versus Q_2 relation between the different compositions in the range 100%-40% SiO_2 (Figure 2). Structural study of these glasses at ambient pressure emphasizes a similar structure between 40% and 50% SiO_2 , as structural changes from MgSiO_3 to Mg_2SiO_4 are concentrated between 33% and 37% SiO_2 (Wilding et al. 2004).

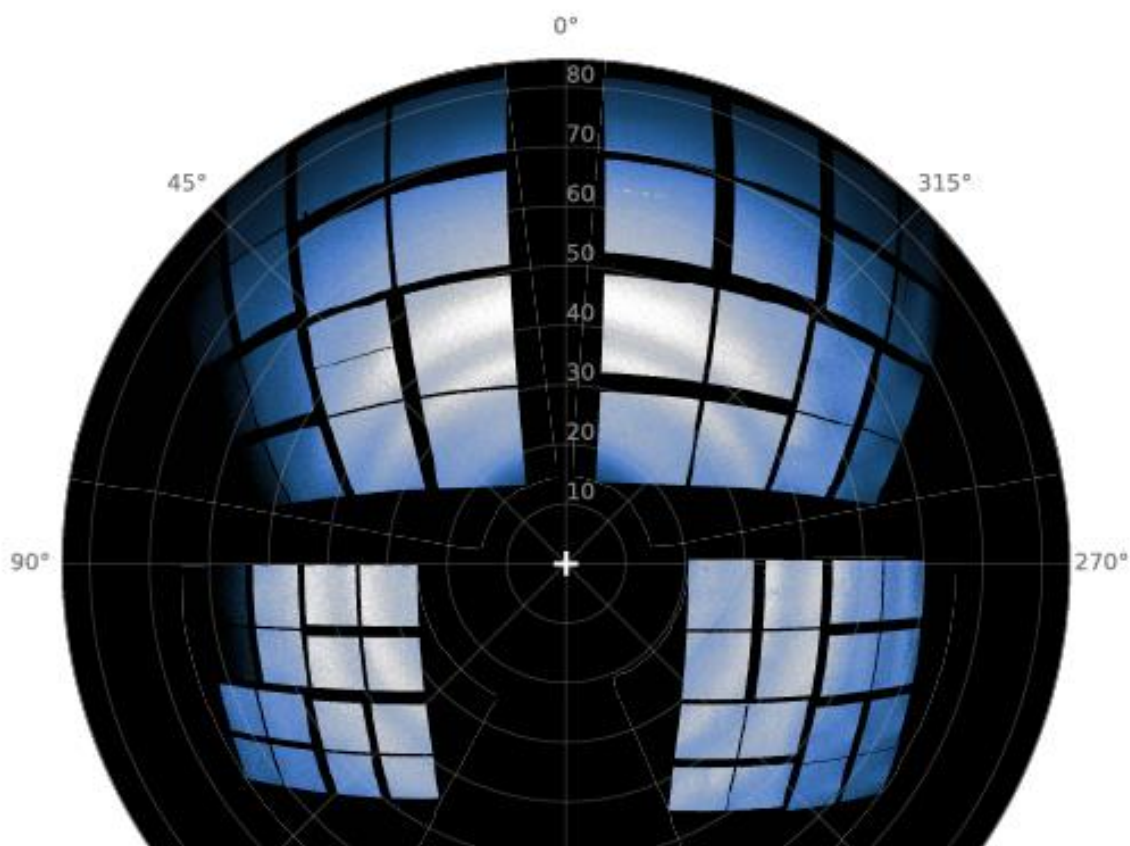


Figure S8: Image plates of shot #96 (MgSiO_3 glass at 129 GPa) projected in the 2 θ -angle-azimuth plane. No diffraction peaks or lines are visible on any of the four image plates of the CSPAD. The intensity levels have been adjusted independently for each CSPADs. CSPAD discontinuities and other masked regions are interpolated on the integrated pattern, largely improving its smoothness.

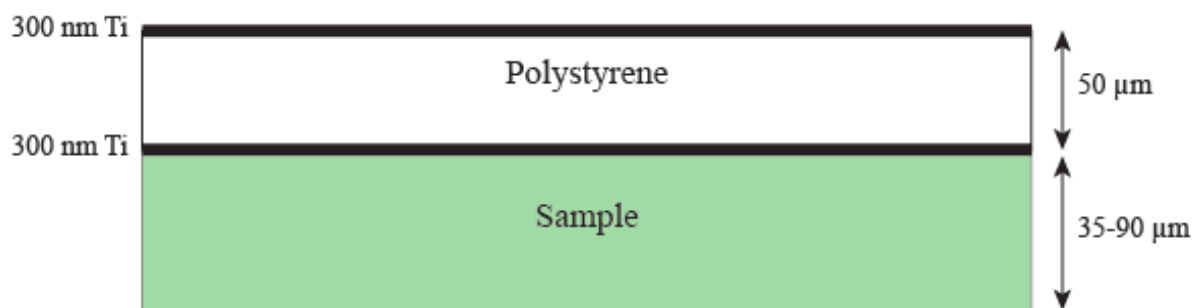


Figure S9: Schematic drawing of a laser shock target.

Supplementary information on laser-shock compression VISAR analysis

In our experiments, the laser spatial profile has been smoothed by the use of continuous phase plates (CPP), producing a uniform 250 μm diameter focal spot. Eventual remaining heterogeneities are then additionally smoothed in the propagation of the shock through the thick 50 μm plastic ablator. Two-dimensional effects in the shock propagation were not substantial in our experiment, as the whole target thickness ($< 100 \mu\text{m}$) was much smaller than the focal spot (250 μm), which in turn was much larger than the spatial extent of the x-ray probe beam ($< 50 \mu\text{m}$). Alignment between the x-ray beam and the optical laser was checked before each shot.

The estimation of the shock pressure reached in each shot has been obtained from the measurement of either shock velocity or particle velocity and considering the known equation of state of MgSiO_3 glass from previous works (2, 3).

To ensure a good quality for the XRD patterns, it is crucial to probe uniform compression conditions with x-rays. To address this issue, we have optimized the experimental configuration, including pusher geometry and target thickness using hydrodynamic simulations. The thickness of the pusher was chosen in such a way to promote shock steadiness by delaying the arrival of the relaxation wave from the front-side plastic, while keeping 2D effects negligible. To confirm simulation predictions and verify the shock steadiness in the actual experiment we have used various target geometries to access different velocity measurements, including mean shock velocity, particle velocity at the shock entrance into the silicate and at its exit. The pressure value deduced by these different approaches are in agreement within the error bars, giving us confidence on the pressure determined in each shot. These tests were conducted for different silicate samples - on an ensemble of data much wider than the set of shots on MgSiO_3 glass presented in this work.

In the following, we give some example of the VISAR data and the related analysis. For low laser energy, the shock is weak enough and the sample is left transparent. In this case our target design allows particle velocity measurement with VISAR, considering the variation of the MgSiO_3 refractive index with pressure (6, 11). This gives us a sound estimation of the pressure transmitted in the sample. In this case the mean shock velocity can also be measured, as the shock breakout time was detected in the VISAR images. While this is not generally the case, in MgSiO_3 the variation rate of the optical length induced by the shock breakout is large enough to affect the interference pattern, producing a peculiar fringe shift in the VISAR image. To illustrate this point, in [Figure S10](#), we show a synthetic VISAR image for such a case. The time dependent interference (phase difference) has been calculated by using the Ti/silicate interface velocity from the hydrodynamic simulations output and considering the density variation of the refractive index with density. The hydrodynamic simulation was calibrated using the value of the interface velocity measured in the experiment and has been run using the actual pulse shape. The shock breakout is evidenced as a very peculiar change in slope in the fringes ([Figure S10](#)).

The synthetic image reproduces the main features we find in the VISAR images for transparent shots, giving us confidence in the interpretation of the signal. We emphasize that the independent measurement of particle and mean shock velocity is carried out

without any intent to furnish quantitative analysis, but rather to take advantage of the VISAR data for characterization the shock propagation and steadiness.

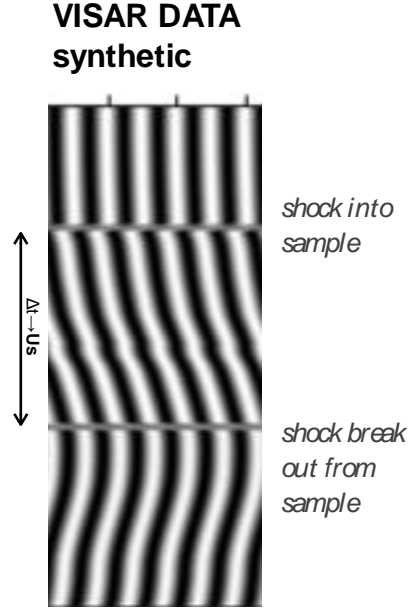


Figure S10: Synthetic VISAR image for a weak shock leaving the sample transparent, showing the peculiar fringe-shift induced by the shock breakout.

An example of how this procedure is applied to the analysis of the VISAR image for a shot on MgSiO_3 glass kept transparent is reported in [Figure S11](#). The particle velocity at the shock break into the silicate is clearly measurable and the two VISAR traces show a quite stable velocity over almost the whole transit time. The pressure inferred from the measured particle velocity is 36 ± 8 GPa. The peculiar fringe shift related to the shock breakout is also detectable and allows for an estimation of the mean shock velocity, indicating a pressure of 31 ± 11 GPa. The good agreement in the two pressure estimations indicates that the shock is only slightly decaying. In the paper, in cases like this one, where we have both U_s and U_p measurement, the pressure value is calculated through the Rankine-Hugoniot equation and the error is estimated using Monte-Carlo methods as describe in the Methods section. For the case considered before, this approach gives $P = 34 \pm 8$ GPa.

In the VISAR image of [Figure S11](#), the XFEL arrival is also visible as a change in the reflectivity of the thin Ti layer. This is used to verify the good probing time.

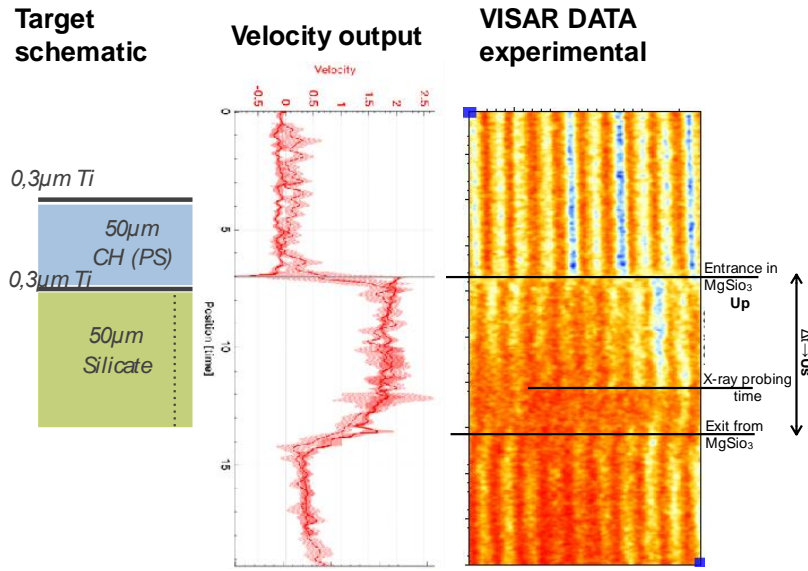


Figure S11: Example of VISAR analysis in the case the silicate is kept transparent.

For stronger shocks, the silicate is turned opaque or slightly reflective (reflectivity of few %, not measurable in our set-up) and the shock transit time is used to get information on the mean shock velocity.

Using confocal imagery and interferometry we have measured the thickness of each sample and selected only those thinner than 57 μm . Planarity could also be characterized with 100nm accuracy, so that the known thickness variation could have been used in the error estimation. Typical thickness variation is of the order of 1.5 μm . To verify shock steadiness, we have also conducted additional shots using a 0.3 μm Ti coated LiF window at the silicate rear side to precisely measure particle velocity at the rear side. In order to not affect the measurement, the window was not glued, but attached with a thin (300 nm) formvar membrane. Within error bars, the pressure inferred with this measurement is in agreement with the values obtained from mean shock velocities at the same laser energy.

An example of the VISAR measurement in this case is given in the following **Figure S12**.

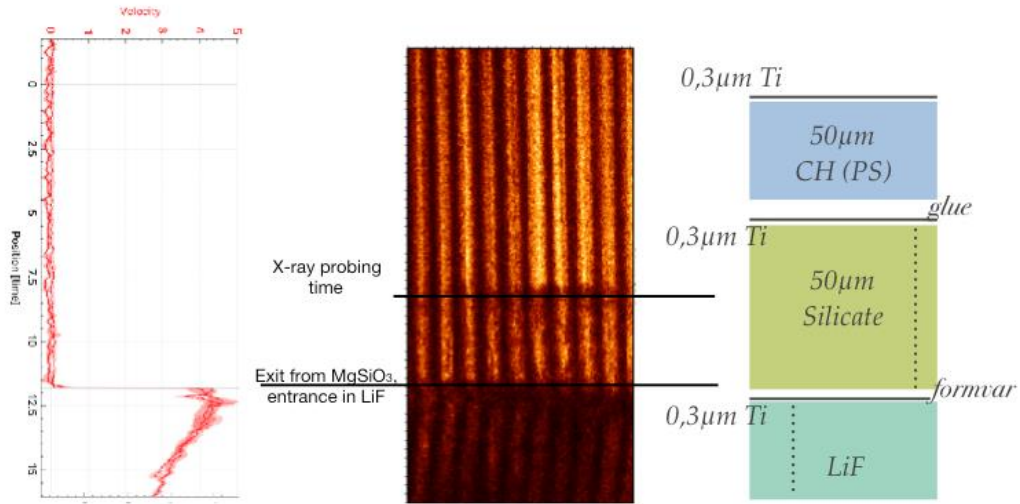


Figure S12 : Example of transit time analysis for high intensity shock

The laser temporal shapes have been recorded for each shot and the actual profile has been used in hydrodynamic simulations to verify that no substantial issues with shock steadiness were induced. Two representative pulse shapes for different laser energies as recorded in the experiment are shown in **Figure S13**.

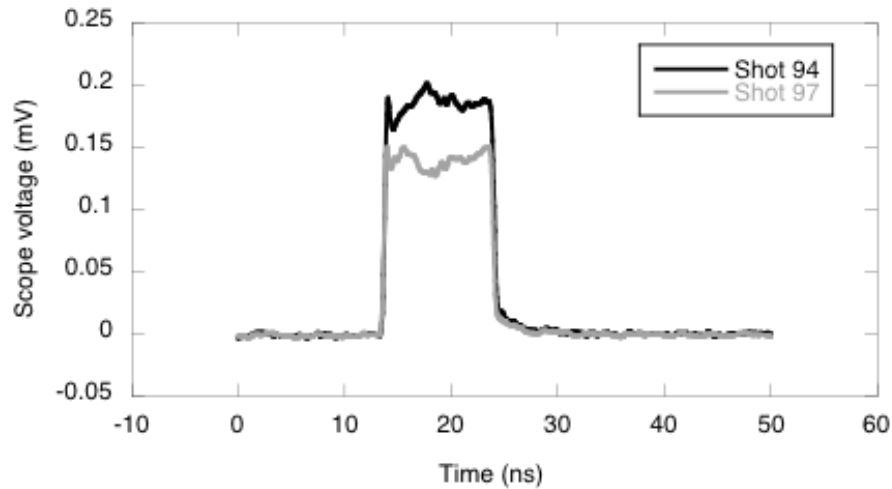


Figure S13: Representative pulse shape for different laser energies. Two representative pulse shapes for different laser energies as recorded in the experiment, showing the good reproducibility on rise time and duration.

MgSiO₃ glass

Shot #	Q1 (nm ⁻¹)	std Q1	Q2 (nm ⁻¹)	std Q2	P (GPa)	std P	ρ (g.cm ⁻³)	std ρ
95	26.96	0.10	34.22	0.18	124	32	4.939	1.285
96	27.35	0.13	34.54	0.29	129	35	4.996	1.385
97	26.96	0.23	33.59	0.25	80	8	4.847	0.602
98	26.18	0.03	32.51	0.05	59	9	4.128	0.325
99	25.33	0.13	31.29	0.21	34	8	4.029	0.419
100	24.73	0.14	-	0.10	24	5	3.682	0.586

Table S1: Summary of peaks positions for shock compressed MgSiO₃ glasses fitted on diffuse XRD patterns. Uncertainties on the positions are calculated from an average of the four images plates used in the standard diffraction geometry at MEC end station, LCLS. Pressure and error bars are calculated from VISAR measurements, when available. Density is given by the EoS used to retrieve the position on the Hugoniot.

SiO₂ glass

Shot #	Q1 (nm ⁻¹)	std Q1	Q2 (nm ⁻¹)	std Q2	P (GPa)	std P	ρ (g.cm ⁻³)	std ρ
58	21.63	1.00	-	-	26	1	4.105	0.170
62	24.93	0.23	33.91	0.21	89	6	4.720	0.098
63	24.93	0.50	-	-	-	-	-	-
64	24.73	0.32	33.40	0.14	-	-	-	-

Table S2: Same as previous for experiments starting with fused silica.

MgSiO₃ DAC 300 K (ESRF-ES650)

P (GPa)	Q1 (nm⁻¹)	Q2 (nm⁻¹)
2.94	20.92	
4.32	22.08	
8.14	22.80	
10.32	23.14	
12.22	23.75	29.11
13.42	24.10	29.87
16.89	24.44	30.42
18.42	24.79	31.18
24.90	25.14	31.47
29.60	25.23	31.64
33.48	25.56	32.08
36.69	25.71	32.28
40.30	25.83	32.70
44.05	25.99	32.65
46.61	26.22	33.02
50.33	26.27	33.08
53.73	26.52	33.62
54.83	26.53	33.77
60.43	26.74	33.74
67.43	26.78	33.98
69.48	26.72	33.97
71.85	26.83	34.11
74.06	26.87	34.24
76.23	26.92	34.26
79.29	26.91	34.24
81.82	27.00	34.37
82.94	27.03	34.38
87.44	27.12	34.48
91.67	27.20	34.64
95.72	27.31	34.71
96.76	27.21	34.75

Table S3: Summary of DAC measurements performed on the High Pressure ID27 beamline at the ESRF, Grenoble. For this run, we used the MCC set-up available on the beamline (14), to reduce the background signal from the sample and obtain high quality diffuse scattering for cold compressed MgSiO₃ glass. Pressure was calibrated using the EoS of KCl (15) from a chip located on the side of the sample, with an error bar estimated at ± 0.5 GPa. Error on the peak position is estimated to be ± 0.1 nm⁻¹.

MgSiO₃ High Pressure dataset		
P (GPa)	Q1 (nm⁻¹)	Q2 (nm⁻¹)
78.0	26.98	33.90
77.9	27.03	33.64
80.7	27.05	33.63
85.2	26.92	33.99
93.5	27.06	34.42
97.4	27.01	34.10
105.9	27.18	33.69
109.8	27.25	34.43
117.1	27.57	34.63
120.1	27.84	35.09
122.9	27.92	35.21
129.1	27.87	35.17
132.9	27.75	35.26
138.1	27.85	35.16
142.1	27.87	35.27
144.8	28.09	35.31
150.7	28.21	35.37
155.9	28.26	35.36
157.0	28.27	35.40

***Table S4:** Summary of the High Pressure run performed on the High Pressure ID27 beamline at the ESRF, Grenoble. Unfortunately, this serie of measurements has not been done with the MCC setup. Pressure was calibrated using Re gasket EoS (1) collected at the same time at the sample signal. Due to the non-hydrostatic stress, and to the fact the Re is located outside the pressure chamber, we estimate the error on pressure to be ± 5 GPa. Error on the peak position is estimated to be $\pm 0.2 \text{ nm}^{-1}$, higher than the LP run due to the lowest signal quality.*

Mg₃Si₂O₇ glasses

Shot #	Q1 (nm ⁻¹)	Q2 (nm ⁻¹)	std Q1 (nm ⁻¹)	std Q2 (nm ⁻¹)
145	27.655	34.882	0.054	0.143
150	24.953	30.457	0.067	0.042
152	26.054	32.618	0.076	0.180
146	27.599	34.412	0.137	0.255
148	26.079	32.766	0.163	0.222
149	26.397	33.445	0.111	0.237
153	26.391	32.865	0.122	0.162
155	25.898	31.986	0.098	0.163
156	25.340	30.681	0.070	0.226

Table S5: Summary of peaks positions for shock compressed Mg₃Si₂O₇ glasses fitted on diffuse XRD patterns. Uncertainties on the positions are calculated from an average of the four images plates used in the conventional diffraction geometry at MEC end station, LCLS. As no Hugoniot is available for this type of sample, the pressure could be measured using VISAR.

P (GPa)	T (K)	ρ (g.cm ⁻³)	Q1 (nm ⁻¹)	Q2 (nm ⁻¹)	Mean Si-O CN
90	4000	4.746	26.424	33.201	6.1
120	6000	4.906	26.608	33.762	6.3
120	4000	5.051	26.947	33.977	6.5
170	6000	5.348	27.347	34.714	6.7

Table S6: Pressure and Temperature conditions for the molecular dynamics simulations.

References

1. Anzellini S, Dewaele A, Occelli F, Loubeyre P, Mezouar M (2014) Equation of state of rhenium and application for ultra high pressure calibration. *J Appl Phys* 115(4).
2. Luo SN, Akins JA, Ahrens TJ, Asimow PD (2004) Shock-compressed MgSiO₃ glass, enstatite, olivine, and quartz: Optical emission, temperatures, and melting. *J Geophys Res Solid Earth* 109(5):1–14.
3. Akins JA, Luo SN, Asimow PD, Ahrens TJ (2004) Shock-induced melting of MgSiO₃ perovskite and implications for melts in Earth's lowermost mantle. *Geophys Res Lett* 31(14):2–5.
4. Mosenfelder JL, Asimow PD, Frost DJ, Rubie DC, Ahrens TJ (2009) The MgSiO₃ system at high pressure: Thermodynamic properties of perovskite, postperovskite, and melt from global inversion of shock and static compression data. *J Geophys Res Solid Earth* 114(1):1–16.
5. Spaulding DK, et al. (2012) Evidence for a phase transition in silicate melt at extreme pressure and temperature conditions. *Phys Rev Lett* 108(6):1–4.
6. Bolis RM, et al. (2016) Decaying shock studies of phase transitions in MgO-SiO₂ systems: Implications for the super-Earths' interiors. *Geophys Res Lett* 43(18):9475–9483.
7. de Koker N, Stixrude L (2009) Self-consistent thermodynamic description of silicate liquids, with application to shock melting of MgO periclase and MgSiO₃ perovskite. *Geophys J Int* 178(1):162–179.
8. Zerr A, Bohler R (1993) Melting of (Mg , Fe) SiO₃ Perovskite to 625 Kilobars : Indication of a High Melting Temperature in the Lower Mantle. *Science* (80-) 262(October):553–555.
9. Sweeney JS, Heinz DL (1993) Melting of iron-magnesium-silicate perovskite. *Geophys Res Lett* 20(9):855–858.
10. Heinz DL, Jeanloz R (1987) Measurement of the Melting Curve of Mg_{0.9}Fe_{0.1}SiO₃ at Lower Mantle Conditions and Its Geophysical Implications. *J Geophys Res, Solid Earth* 92(B11):11437–11444.
11. Fratanduono DE, et al. (2018) Thermodynamic properties of MgSiO₃ at super-Earth mantle conditions. *Phys Rev B* 97(21):214105. Available at: <https://link.aps.org/doi/10.1103/PhysRevB.97.214105>.
12. Belonoshko AB, et al. (2005) High-Pressure Melting of MgSiO₃. *Phys Rev Lett* 195701(May):20–23.
13. Tateno S, Hirose K, Sata N, Ohishi Y (2009) Determination of post-perovskite phase transition boundary up to 4400 K and implications for thermal structure in D'' layer. *Earth Planet Sci Lett* 277(1–2):130–136. Available at: <http://dx.doi.org/10.1016/j.epsl.2008.10.004>.
14. Weck G, et al. (2013) Use of a multichannel collimator for structural investigation of low-Z dense liquids in a diamond anvil cell: Validation on fluid H₂ up to 5 GPa. *Rev Sci Instrum* 84(6).
15. Dewaele A, et al. (2012) High-pressure-high-temperature equation of state of KCl and

KBr. *Phys Rev B - Condens Matter Mater Phys* 85(21):1–7.